A COMPRESSIVE SENSING APPROACH FOR SYNTHETIC APERTURE IMAGING RADIOMETERS

Shiyong Li[1, *], Xi Zhou[2], Bailing Ren[1], Houjun Sun[1], and Xin Lv[1]

[1]School of Information and Electronics, Beijing Institute of Technology, Beijing 100081, China

[2]China Academy of Space Technology, Beijing 100081, China

Abstract—The aperture synthesis technology represents a promising new approach to microwave radiometers for high-resolution observations of the Earth from geostationary orbit. However, the future application of the new technology may be limited by its large number of antennas, receivers, and correlators. In order to reduce significantly the complexity of the on-board hardware requirements, a novel method based on the recently developed theory of compressive sensing (CS) is proposed in this paper. Due to the fact that the brightness temperature distributions of the Earth have a sparse representation in some proper transform domain — for example, in terms of spatial finite-differences or their wavelet coefficients, we use the CS approach to significantly undersample the visibility function. Thus the number of antennas, receivers, and correlators can be further reduced than those based on the traditional methods that obey the Shannon/Nyquist sampling theorem. The reconstruction is performed by minimizing the ℓ_1 norm of a transformed image. The effectiveness of the proposed approach is validated by numerical simulations using the image corresponding to AMSU-A over the Pacific.

1. INTRODUCTION

Microwave radiometers are powerful sensors for high-resolution observations of the Earth at relatively low frequencies [1, 2]. The low microwave frequency range offers high penetration ability through clouds and into the top layer of the Earth surface. However, it has the specific disadvantage of poor spatial resolution which is attained with

moderately sized antennas. For imaging from space at low microwave frequencies, large antenna apertures of up to 10 m or more can be normally required which means serious problems for any practical mechanically or electronically steered antennas [3].

Interferometric aperture synthesis, initially developed for radio astronomy [4], can be an effective alternative to real aperture radiometers for the Earth observation. It has been implemented and successfully demonstrated with ESTAR and SMOS sensors [5, 6]. Synthetic aperture radiometers measure the correlation between pairs of nondirective antennas. Each complex correlation is a sample of the "visibility" function which, in the ideal case, is the spatial Fourier transform of the brightness temperature distribution [5]. Thus the choice of the antenna array shape is of great importance because it determines the sampling strategy in the frequency domain. Several kinds of antenna configuration such as T-, U-, Y-, and triangular shaped arrays have been used for synthetic aperture radiometers. For the T- and U-shaped arrays, the visibility samples lie in a rectangular grid in the frequency domain (u, v). And for the Y- and triangular-shaped arrays, the visibility samples lie in a hexagonal grid. All the aforementioned arrays give uniform distributed samples in the frequency domain and the brightness temperature reconstruction is based on the rectangular fast Fourier transform (FFT). However, there are many redundant baselines for the aforementioned arrays. The future application of this new technology is limited by its large number of antennas, receivers, and correlators. In order to reduce the complexity of the on-board hardware requirements, the circular and rotating array configurations with minimum redundancy have been proposed [7, 8]. However, their disadvantages lie primarily in more complicated image reconstruction. As the samples measured by these arrays are distributed in the nonuniform grid, the FFT-based method could not be directly used. A common way for image reconstruction is the gridding method [9]. The nonuniformly sampled data are first interpolated to a uniform Cartesian grid, and then, the inverse Fourier transform is efficiently computed using FFT to reconstruct the image. However, this approach is liable to introduce inaccuracies and is sensitive to the distribution of the samples.

In [10], an iterative method that combines the Conjugate Gradient (CG) algorithm with NUFFT operations was applied to reconstruct the image from the nonuniform visibility samples. The results demonstrate that the proposed algorithm has the advantage of better reconstruction accuracy than the traditional gridding method. However, only the imaging accuracy was discussed in [10]. The design of mean distance between adjacent samples was still according to Shannon/Nyquist

sampling theorem.

In order to reduce further the complexity of the antenna array and receiver channels, we apply the compressive sensing theory to the synthetic aperture imaging radiometers (SAIRs) design. The recently introduced theory of *compressive sensing/compressed sensing* (CS) states that a signal having a sparse representation can be recovered exactly from a small set of linear, non-adaptive measurements [11–14]. It has been explored for a wide range of applications, such as: medical imaging [15–18], radar imaging [19–26], sub-Nyquist sampling systems [27, 28], channel coding [29, 30], single-pixel cameras [31], and etc.. CS imaging techniques for radio astronomy application have been proposed in [32] and [33].

Due to the fact that CS can be used for sensing and compressing data simultaneously, the antenna array of the SAIRs can be compressed by using the CS approach in some conditions. In this paper, we first design a circular array with fewer antennas (and receivers) than the traditional ones. Then we apply the CS approach to reconstruct the brightness temperature image. To our knowledge, the image reconstruction of the SAIRs has not been considered from the point of view of CS theory before. CS gives a new perspective on inverse problems with random measurements. Randomness is a powerful tool for using CS successfully. The randomness in the visibility distribution of the circular array complies exactly with the CS requirements. Thus the brightness temperature images can be reconstructed with higher accuracy from only fewer visibilities compared with the results obtained by traditional methods.

The rest of this paper is organized as follows. In Section 2, we briefly review the concepts of CS and introduce CS approach to SAIRs. Simulation results are given in Section 3. And Section 4 presents the conclusions.

2. COMPRESSIVE SENSING FOR SAIRS

2.1. Principles of CS

This section gives briefly the theoretical fundamentals of CS, as introduced in [13]. The area of CS was initiated in 2006 by two ground breaking papers by Candès, Romberg, and Tao [11], and by Donoho [12]. The key idea of CS is to reconstruct a sparse signal from very few non-adaptive, linear measurements by convex optimization.

Consider a finite signal $x \in \mathbb{R}^N$ and a limited number of observations of x in the form of M linear measurements, we can

represent this process mathematically as

$$y = \Phi x, \tag{1}$$

where Φ is an $M \times N$ matrix, and $y \in \mathbb{R}^M$. The matrix Φ represents a dimensionality reduction, where M is typically much smaller than N, i.e., the system of equations in (1) is highly underdetermined.

If x is sparse (or has a sparse expansion in a proper basis), it is quite intuitive to recover x from knowledge of y by solving the ℓ_0 norm (the number of its non-zero components) minimization problem which, however, needs the combinatorial search that is NP-hard [34].

One approach for translating this problem into something more tractable is to replace ℓ_0 norm with its convex relaxation ℓ_1 norm. It has been shown in the context of CS theory that it is very likely to recover x exactly from the ℓ_1-minimization problem provided that x is sparse and that the sensing matrix Φ obeys the *restricted isometry property* (RIP) [11]. The RIP is related to the incoherence of the sets of columns of the sensing matrix, i.e., for K-sparse signals all subsets of K columns taken from Φ are in fact nearly orthogonal [13].

If the RIP holds, then the following linear program gives an accurate reconstruction of x:

$$\min_{x \in \mathbb{R}^N} \|x\|_{\ell_1}, \qquad \text{subject to } y = \Phi x, \tag{2}$$

where $\|x\|_{\ell_1} = \sum |x_i|$ represents the ℓ_1 norm of x, and x_i is the ith component of x.

For many natural signals which are not sparse and, however, often have concise representations in a convenient basis, i.e., $x = \Psi \alpha$, where α is a sparse vector, and then (2) can be reformulated as:

$$\min_{x \in \mathbb{R}^N} \|\alpha\|_{\ell_1}, \qquad \text{subject to } y = \Phi \Psi \alpha, \tag{3}$$

where $\alpha = \Psi^{-1} x$.

A related condition for (3), known as incoherence, requires that the rows of Φ cannot be represented by the columns of Ψ and vice versa [13]. Designing the matrix Φ such that the resulting sensing matrix $\Theta = \Phi \Psi$ has the RIP is a fundamental problem in CS. In fact, one can show that the RIP can be achieved with high probability by simply selecting Φ as random matrices, such as Gaussian iid matrices, Bernoulli matrices, or random partial Fourier matrices [13], which are largely incoherent with any fixed basis Ψ. For the random partial Fourier matrices, the RIP holds with overwhelming probability if $K \leq C \cdot M / \log N$ [13]. However, the RIP or the incoherence condition is likely to be some conservative for many cases. Even though some signals do not satisfy the condition of RIP, the reconstruction may still be accurate [35].

The computation of (2) or (3) is a convex optimization problem, and can be solved efficiently using linear programming methods. This is the foundation for the Basis Pursuit (BP) techniques [12]. In the case when there are noisy measurements, Basis Pursuit De-Noising (BPDN) techniques can be used to reconstruct the original signals [36]. Further, convex optimization methods are effective at solving problems in which the signal is not very sparse or heavy observational noise is present. While convex optimization techniques are powerful methods for computing sparse representations, there are also a variety of Greedy methods for solving such problems [37, 38]. Compared with convex optimization methods, Greedy pursuits and related methods (such as iterative thresholding) can be rather fast but need more measurements. However, recent research has clarified that Greedy methods succeed empirically and theoretically in many situations where convex relaxation works. Some Greedy methods can actually have performance guarantees that match those obtained for convex optimization approaches [39]. In this paper, we focus on the convex optimization methods with the application to SAIRs.

2.2. Compressive Sensing Approach Applied to SAIRs

The interferometric radiometers measure the correlation between pairs of spatially separated antennas. Each complex correlation is a sample of the visibility function. According to [40], the visibility samples for any two antennas labeled k and l, is given by

$$V\left(u_{k,l}, v_{k,l}\right) = \iint\limits_{\xi^2+\eta^2<1} T'_{k,l}\left(\xi,\eta\right) e^{-j2\pi\left(u_{k,l}\xi + v_{k,l}\eta\right)} d\xi d\eta, \qquad (4)$$

where $T'_{k,l}(\xi,\eta)$ is the modified brightness temperature:

$$T'_{k,l}(\xi,\eta) = \frac{T(\xi,\eta)}{\sqrt{1-\xi^2-\eta^2}} \cdot \frac{F_k(\xi,\eta)\,F_l^*(\xi,\eta)}{\sqrt{\Omega_k\Omega_l}} \tilde{r}\left(-\frac{u_{k,l}\xi + v_{k,l}\eta}{f_0}\right), \ (5)$$

where $T(\xi,\eta)$ is the brightness temperature, $(\xi,\eta) = (\sin\theta\cos\varphi, \sin\theta\sin\varphi)$ the direction cosines with respect to (x,y) axes as shown in Figure 1, and $(u_{k,l}, v_{k,l}) = (x_k - x_l, y_k - y_l)/\lambda$ the spacing between the two antennas in wavelengths. The $1/\sqrt{1-\xi^2-\eta^2}$ in (5) is the obliquity factor, $F_{k,l}(\xi,\eta)$ is the normalized antenna patterns, $\Omega_{k,l}$ represents the antenna equivalent solid angles, and $\tilde{r}(\cdot)$ denotes the fringe-washing function [41].

In short, image reconstruction consists mainly of solving for $T'(\xi,\eta)$ in an equation of the type $V(u,v) = \mathcal{F}[T'(\xi,\eta)]$, where $\mathcal{F}[\cdot]$ represents the Fourier transform. The selection of image reconstruction

method is based on the distribution of $V(u,v)$ which is determined by the configuration of antenna array. As discussed in Section 1, for U-, T-, Y-, and triangular-shaped arrays, the image reconstruction is based on the use of FFT. And for circular-shaped arrays, the visibility samples lie naturally in random locations, and the gridding methods are commonly used. In this paper, we reconstruct the image based on the CS theory, with the properties of reducing further the number of antennas, receivers, and correlators, and improving the image accuracy in the same time. The visibility function should be formulated as a vector due to the fact that the visibilities lie naturally in random locations for the circular arrays. Thus we rewrite (4) in the following matrix form:

$$vec\left(V\right) = G \cdot vec\left(T'\right), \qquad (6)$$

where

$$
G = \begin{bmatrix}
e^{-j2\pi(u_{0,0}\xi_0+v_{0,0}\eta_0)} & e^{-j2\pi(u_{0,0}\xi_0+v_{0,0}\eta_1)} \\
e^{-j2\pi(u_{0,1}\xi_0+v_{0,1}\eta_0)} & e^{-j2\pi(u_{0,1}\xi_0+v_{0,1}\eta_1)} \\
\vdots & \vdots \\
e^{-j2\pi\left(u_{K-1,L-1}\xi_0+v_{K-1,L-1}\eta_0\right)} & e^{-j2\pi\left(u_{K-1,L-1}\xi_0+v_{K-1,L-1}\eta_1\right)}
\end{bmatrix}
$$

$$
\begin{matrix}
\cdots & e^{-j2\pi(u_{0,0}\xi_0+v_{0,0}\eta_{M-1})} \\
\cdots & e^{-j2\pi(u_{0,1}\xi_0+v_{0,1}\eta_{M-1})} \\
\vdots & \vdots \\
\cdots & e^{-j2\pi\left(u_{K-1,L-1}\xi_0+v_{K-1,L-1}\eta_{M-1}\right)}
\end{matrix}
$$

$$
\begin{matrix}
e^{-j2\pi(u_{0,0}\xi_1+v_{0,0}\eta_0)} & e^{-j2\pi(u_{0,0}\xi_1+v_{0,0}\eta_1)} \\
e^{-j2\pi(u_{0,1}\xi_1+v_{0,1}\eta_0)} & e^{-j2\pi(u_{0,1}\xi_1+v_{0,1}\eta_1)} \\
e^{-j2\pi\left(u_{K-1,L-1}\xi_1+v_{K-1,L-1}\eta_0\right)} & e^{-j2\pi\left(u_{K-1,L-1}\xi_1+v_{K-1,L-1}\eta_1\right)} \\
\cdots & e^{-j2\pi(u_{0,0}\xi_{N-1}+v_{0,0}\eta_{M-1})}
\end{matrix}
$$

$$
\begin{matrix}
\cdots & e^{-j2\pi(u_{0,0}\xi_{N-1}+v_{0,0}\eta_{M-1})} \\
\cdots & e^{-j2\pi(u_{0,1}\xi_{N-1}+v_{0,1}\eta_{M-1})} \\
\vdots & \vdots \\
\cdots & e^{-j2\pi\left(u_{K-1,L-1}\xi_{N-1}+v_{K-1,L-1}\eta_{M-1}\right)}
\end{matrix},
$$

and $vec\left(\cdot\right)$ represents vectorization. Here we assume that the image size is $M \times N$, and visibilities size is $K \times L$.

Clearly, in the case of circular array configuration, the sensing matrix G arises from a random selection of Fourier samples. As mentioned above, we know that the random partial Fourier matrices are highly incoherent with any fixed basis.

The brightness temperature images are generally not sparse in the spatial domain. Thus the sparsifying transforms, such as

the discrete cosine transform (DCT), wavelet transform, and finite-differences transform, are needed to map the images to some sparse forms. When finite-differencing is used as a sparsifying transform, the objective in (3) becomes the well-known problem of Total-Variation (TV) minimization [36].

The TV minimization is widely used in several applications such as image denoising, deblurring, and MRI image recovery [42], mainly due to its desirable properties such as convexity, ability to preserve edges, as well as invariance to image shifts and rotations. The TV norm can be interpreted as the ℓ_1 norm of the gradient. And (3) can be reformulated as

$$\min_{T'} \sum_{i,j} \left| (\nabla T')_{i,j} \right|, \quad \text{subject to } vec(V) = G \cdot vec(T'), \quad (7)$$

where $(\nabla T')_{i,j}$ is given by

$$(\nabla T')_{i,j} = \left[\begin{array}{c} (D_1 T') [i,j] \\ (D_2 T') [i,j] \end{array} \right],$$

and $(D_1 T') [i,j] = T' [i+1, j] - T' [i,j]$, $(D_2 T') [i,j] = T' [i, j+1] - T' [i,j]$.

There are many state-of-the-art optimization methods designed to solve (2), (3) or (7) [43–47]. In this paper, we use an algorithm called NESTA to solve the convex optimization problem of (7). NESTA is developed by Stephen Becker, etc., for solving large-scale problems based on Nesterov's work [48–50]. It is a fast and robust first-order method that solves minimum ℓ_1 problems and a large number of extensions including TV minimization with the accelerated convergence rate of $O(1/k^2)$.
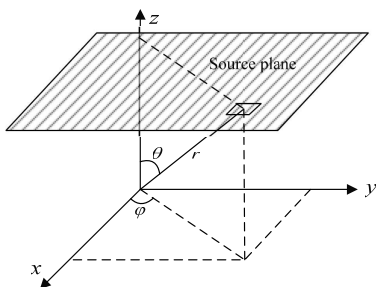

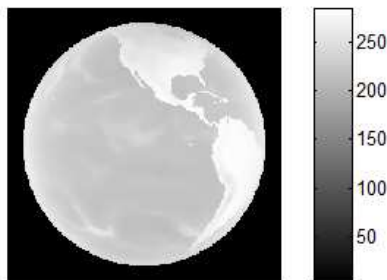**Figure 1.** Geometry of the synthetic aperture radiometers and related terms.

Figure 2. Original brightness temperature image of the Pacific.

3. SIMULATIONS AND RESULTS

In this section, we evaluate the performance of CS approach for SAIRs using the Earth brightness temperature distribution viewed from geostationary orbit. The size of the image is 256×256 pixels, which allows a maximum spatial resolution of 48 km at boresight. The image corresponds to AMSU-A 50.3-GHz channel over the Pacific [51] as shown in Figure 2. Its mean brightness temperature is 226 K, and its standard deviation is 16 K. The dynamic range of the brightness temperature is from 0 to 320 K.

According to the traditional imaging methods, the unambiguous field of view is determined by the smallest spacing of the sampled grid. Then for the 17.5° Earth diameter (as viewed from geostationary orbit) field of view, the mean distance between adjacent uv points is about 3.5 wavelengths. Therefore, in [10] a 120-element circular array with radius of 70 wavelengths was used for the simulation. In this paper, we also set the radius of the array to be 70 wavelengths, and however, the number of array elements to be varied from 120 to 70 with step of minus 10. And the arrays configuration is optimized by the simulated annealing algorithm. This algorithm maximized the mean distance between uv points as a means to acquire the least redundant uv spacing. The baseline redundancy of the optimized result is reduced to zero, and relatively even sampling in spatial frequency domain is achieved. Figure 3 shows the optimized result of a 120-element circular array.

The modified visibilities are computed from the aforementioned original temperature distribution according to the corresponding arrays configuration. As mentioned in Section 2, the NESTA algorithm will be used to reconstruct the images. And the results of the NUFFT-
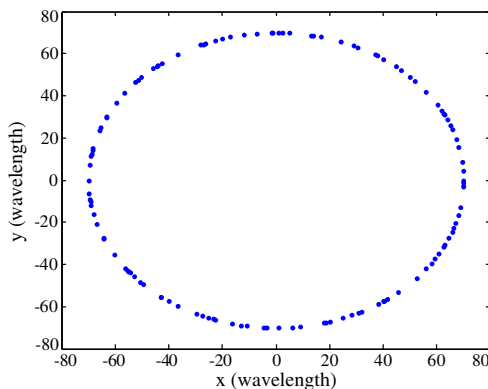

Figure 3. Configuration of a 120-element circular array.

based iterative methods with quadratic penalty and hyperbolic penalty, respectively, are also given for comparisons, which have been demonstrated with higher accuracies than the traditional linear interpolation and gridding methods [10]. The NUFFT-based iterative methods that combine the CG algorithm with NUFFT operations have been used in MRI [52], modern tomographic systems [53], and synthetic aperture imaging radiometers [10].

We notice that the NUFFT-based iterative method with hyperbolic penalty can also be used for signal recovery based on the CS theory. The NUFFT-based iterative method with hyperbolic penalty can be expressed as:

$$\min_{T'} \left\{ F(T') = \frac{1}{2} \left\| vec(V) - G \cdot vec(T') \right\|_{\ell_2} + \lambda \left\| \varphi \left\{ \nabla [vec(T')] \right\} \right\|_{\ell_1} \right\}, \quad (8)$$

where T' is the modified brightness temperature as defined in (5), and the hyperbolic penalty function is given by

$$\varphi(x) = \delta \left[\sqrt{1 + (x/\delta)^2} - 1 \right], \quad (9)$$

where δ is the parameter to tune how much edge-preserving we need.

The hyperbolic functions with $\delta = 0.2$ and $\delta = 1$ are shown in Figure 4, in which the ℓ_1 norm is also demonstrated for comparison. It can be seen from Figure 4 that the hyperbolic penalty function is ℓ_2 like for small variables (i.e., for x in (9)) and ℓ_1 like for large ones which has also been called the "hybrid norm". The hybrid norm is useful in some cases where the tiny residuals have an effect as large as big ones, such as for the geophysical applications [54]. Clearly, the hyperbolic
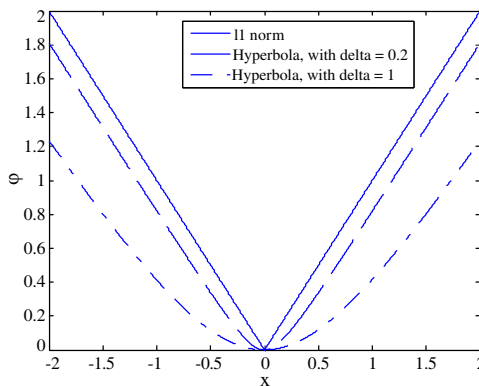

Figure 4. Hyperbolic function and the ℓ_1 norm, where the real line represents ℓ_1 norm, and "- - -" and "$- \cdot -$" lines represent Hyperbolic functions with $\delta = 0.2$ and $\delta = 1$, respectively.
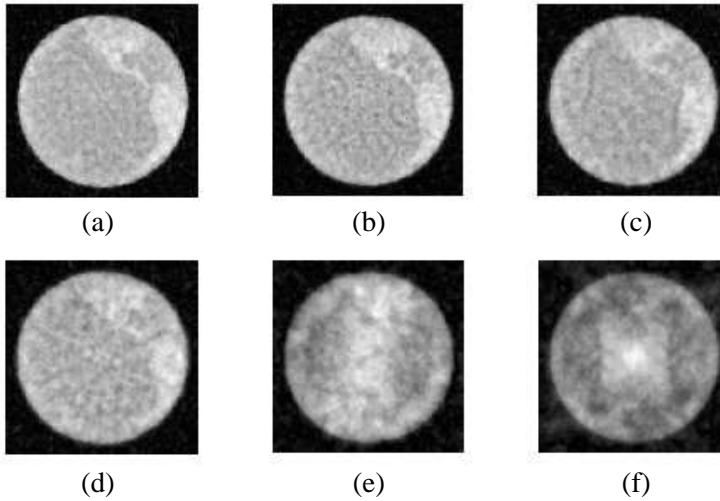
Figure 5. Reconstructed brightness temperature image by the NUFFT-based iterative method with quadratic penalty. The number of array elements is varied from 120 to 70, related to (a) to (f).
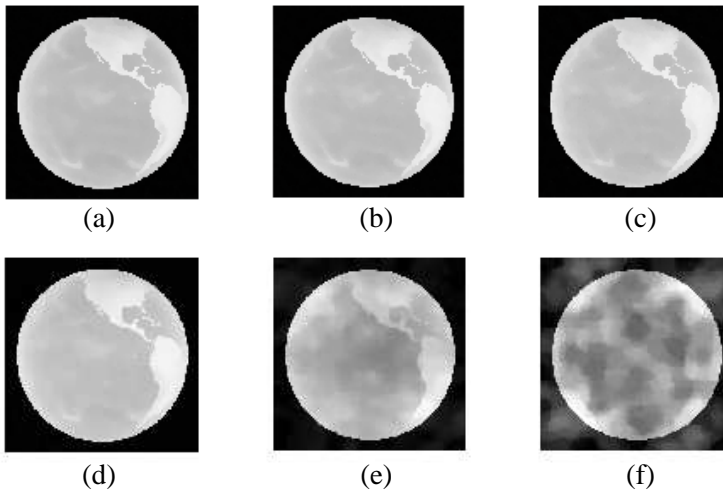

Figure 6. Reconstructed brightness temperature image by the NUFFT-based iterative method with hyperbolic penalty. The number of array elements is varied from 120 to 70, related to (a) to (f).
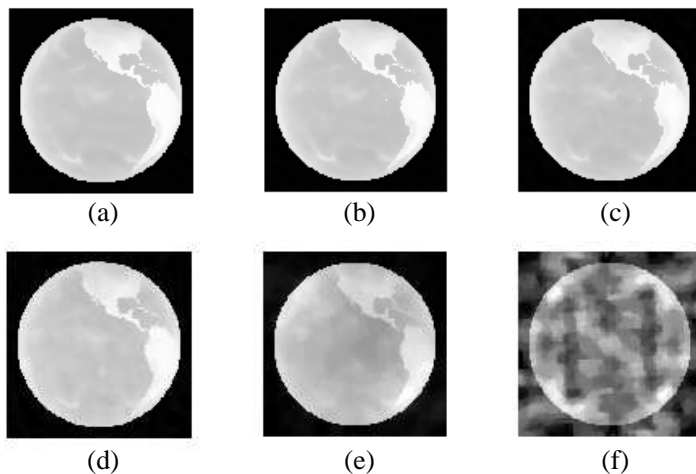
Figure 7. Reconstructed brightness temperature image by the NESTA method. The number of array elements is varied from 120 to 70, related to (a) to (f).

penalty can be used for sparse signal recovery in the framework of CS due to its ℓ_1 norm similarity.

The reconstructed images are shown in Figures 5 to 7 by using the NUFFT-based iterative methods with quadratic penalty and hyperbolic penalty, and the NESTA method, respectively. The parameter δ of the hyperbolic penalty is set to be 0.2. The number of the array elements varies from 120 to 70 related to the corresponding images from (a) to (f). Clearly, the image results of the NUFFT-based method with hyperbolic penalty and the NESTA method are both more accurate than the results of the method with quadratic penalty due to the fact that the first two methods utilize the properties of ℓ_1 norm (or hybrid norm) minimization. When the number of array elements is reduced to 70, the errors of the three methods are all high.

In order to evaluate quantitatively the accuracies of the three methods, we define the relative root-mean square error (RMSE) as follows

$$\text{RMSE} = \frac{\sqrt{\sum_i \left[\widehat{T}'(\xi_i, \eta_i) - T'(\xi_i, \eta_i)\right]^2}}{\sqrt{\sum_i \left[T'(\xi_i, \eta_i)\right]^2}}, \tag{10}$$
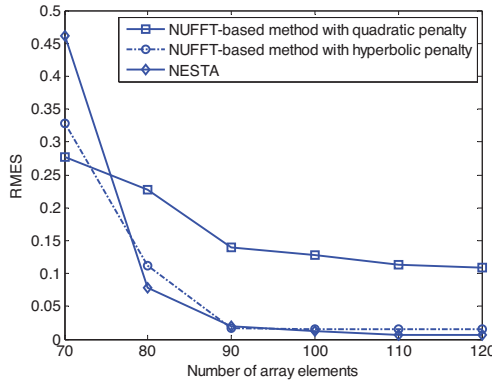
Figure 8. RMSEs of the NUFFT-based methods with quadratic penalty and hyperbolic penalty, and the NESTA method, versus different number of array elements.

where $\widehat{T}'(\xi, \eta)$ is the reconstructed image and $T'(\xi, \eta)$ is the original one.

The RMSEs of the aforementioned three methods are demonstrated in Figure 8. Clearly, the RMSEs of the NUFFT-based method with hyperbolic penalty and the NESTA method are both much lower than the NUFFT-based method with quadratic penalty when the number of array elements is equal to or larger than 80. And the differences between the NUFFT-based method with hyperbolic penalty and the NESTA method are very small.

4. CONCLUSIONS

In this paper, we have proposed a new framework for synthetic aperture imaging radiometers by using the theory of CS. The randomness in the visibility distribution of the circular array complies exactly with the CS requirements. In the framework of CS, the visibility function can be significantly undersampled. Thus the number of antennas, receivers, and correlators of the SAIRs can be further reduced than those based on the traditional methods that obey the Shannon/Nyquist sampling theorem. Numerical simulations of the image corresponding to AMSU-A over the Pacific have demonstrated that a more accurate reconstruction of the brightness temperature distribution can be achieved based on the CS theory than the results obtained by the traditional methods.

Further works to improve the efficiency and real-time implementation of the CS method are underway.

ACKNOWLEDGMENT

REFERENCES

1. Bonafoni, S., F. Alimenti, G. Angelucci, and G. Tasselli, "Microwave radiometry imaging for forest fire detection: A simulation study," *Progress In Electromagnetics Research*, Vol. 112, 77–92, 2011.
2. Giamalaki, M. I. and I. S. Karanasiou, "Enhancement of a microwave radiometry imaging system's performance using left handed materials," *Progress In Electromagnetics Research*, Vol. 117, 253–265, 2011.
3. Kraft, U. R., "Two-dimensional aperture synthesis radiometers in a low earth orbit mission and instrument analysis," *IEEE International Geoscience and Remote Sensing Symposium*, Vol. 2, 866–868, 1996.
4. Le Vine, D. M. and J. C. Good, "Aperture synthesis for microwave radiometers in space," NASA Tech. Memo. 85033, Goddard Space Flight Center, Greenbelt, MD, Aug. 1983.
5. Camps, A., J. Bará, I. C. Sanahuja, and F. Torres, "The processing of hexagonally sampled signals with standard rectangular techniques: Application to 2-D large aperture synthesis interferometric radiometers," *IEEE Trans. Geoscience and Remote Sensing*, Vol. 35, No. 1, 183–190, Jan. 1997.
6. Anterrieu, E., P. Waldteufel, and A. Lannes, "Apodization functions for 2-D hexagonally sampled synthetic aperture imaging radiometers," *IEEE Trans. Geoscience and Remote Sensing*, Vol. 40, No. 12, 2531–2542, Dec. 2002.
7. He, B. Y. and J. Wu, "Two dimensional least redundant array for interferometric synthetic aperture radiometer," *IEEE International Geoscience and Remote Sensing Symposium*, Vol. 7, 4371–4373, 2003.
8. Wu, J., H. Liu, B. Y. He, and W. Y. Sun, "The rotate mother & son satellite system for passive microwave imaging," China Patent, App. No. 200510123633.2, Pub. CN1782734, Nov. 18, 2005.
9. Jackson, J. I., C. H. Meyer, D. G. Nishimura, and A. Macovski, "Selection of a convolution function for Fourier inversion using

gridding," *IEEE Trans. Medical Imaging*, Vol. 10, No. 3, 473–478, Sep. 1991.

10. Zhou, X., H. J. Sun, J. W. He, and X. Lv, "NUFFT-based iterative reconstruction algorithm for synthetic aperture imaging radiometers," *IEEE Geoscience and Remote Sensing Letters*, Vol. 6, No. 2, 273–276, Apr. 2009.

11. Candès, E. J., J. Romberg, and T. Tao, "Robust uncertainty principles: Exact signal reconstruction from highly incomplete frequency information," *IEEE Trans. Information Theory*, Vol. 52, No. 2, 489–509, Feb. 2006.

12. Donoho, D., "Compressed sensing," *IEEE Trans. Information Theory*, Vol. 52, No. 4, 1289–1306, Apr. 2006.

13. Candès, E. J. and M. Wakin, "An introduction to compressive sampling," *IEEE Signal Processing Magazine*, Vol. 25, No. 2, 21–30, Mar. 2008.

14. Eldar, Y. C. and G. Kutyniok, *Compressed Sensing: Theory and Applications*, Cambridge University Press, Cambridge, 2012.

15. Lao, D., M. W. Lenox, and G. Akabani, "The sparsity-promoted solution to the undersampling tof-pet imaging: Numerical simulations," *Progress In Electromagnetics Research*, Vol. 133, 235–258, 2013.

16. Zhang, Y., L. Wu, B. Peterson, and Z. Dong, "A two-level iterative reconstruction method for compressed sensing MRI," *Journal of Electromagnetic Waves and Applications*, Vol. 25, Nos. 8–9, 1081–1091, Jan. 2011.

17. Lustig, M., D. Donoho, and J. M. Pauly, "Sparse MRI: The application of compressed sensing for rapid MR imaging," *Magnetic Resonance in Medicine*, Vol. 58, No. 6, 1182–1195, Dec. 2007.

18. Lustig, M., D. Donoho, J. Santos, and J. Pauly, "Compressed sensing MRI," *IEEE Signal Processing Magazine*, Vol. 25, No. 2, 72–82, Mar. 2008.

19. Wei, S. J., X. L. Zhang, J. Shi, and G. Xiang, "Sparse reconstruction for SAR imaging based on compressed sensing," *Progress In Electromagnetics Research*, Vol. 109, 63–81, 2010.

20. Wei, S. J., X. L. Zhang, and J. Shi, "Linear array SAR imaging via compressed sensing," *Progress In Electromagnetics Research*, Vol. 117, 299–319, 2011.

21. Chen, J., J. Gao, Y. Zhu, W. Yang, and P. Wang, "A novel image formation algorithm for high-resolution wide-swath spaceborne SAR using compressed sensing on azimuth displacement phase

center antenna," *Progress In Electromagnetics Research*, Vol. 125, 527–543, 2012.

22. Li, J., S. Zhang, and J. Chang, "Applications of compressed sensing for multiple transmitters multiple azimuth beams SAR imaging," *Progress In Electromagnetics Research*, Vol. 127, 259–275, 2012.

23. Liu, Z., X. Wei, and X. Li, "Adaptive clutter suppression for airborne random pulse repetition interval radar based on compressed sensing," *Progress In Electromagnetics Research*, Vol. 128, 291–311, 2012.

24. Peng, X., W. Tan, Y. Wang, W. Hong, and Y. Wu, "Convolution back-projection imaging algorithm for downward-looking sparse linear array three dimensional synthetic aperture radar," *Progress In Electromagnetics Research*, Vol. 129, 287–313, 2012.

25. Xing, S., D. Dai, Y. Li, and X. Wang, "Polarimetric SAR tomography using $L_{2,1}$ mixed norm sparse reconstruction method," *Progress In Electromagnetics Research*, Vol. 130, 105–130, 2012.

26. You, Y., H. Xu, C.-S. Li, and L. Zhang, "Data acquisition and processing of parallel frequency SAR based on compressive sensing," *Progress In Electromagnetics Research*, Vol. 133, 199–215, 2013.

27. Gedalyahu, K. and Y. C. Eldar, "Time-delay estimation from low-rate samples: A union of subspaces approach," *IEEE Trans. Signal Processing*, Vol. 58, No. 6, 3017–3031, Jun. 2010.

28. Mishali, M. and Y. C. Eldar, "From theory to practice: Sub-Nyquist sampling of sparse wideband analog signals," *IEEE Journal of Selected Topics in Signal Processing*, Vol. 4, No. 2, 375–391, Apr. 2010.

29. Haupt, J., W. U. Bajwa, G. Raz, and R. Nowak, "Toeplitz compressed sensing matrices with applications to sparse channel estimation," *IEEE Trans. Information Theory*, Vol. 56, No. 11, 5862–5875, Nov. 2010.

30. Hirvonen, T., C. Tzagkarakis, A. Mouchtaris, and P. Tsakalides, "Single-channel and multi-channel sinusoidal audio coding using compressed sensing," *IEEE Trans. Audio, Speech, and Language Processing*, Vol. 19, No. 5, 1382–1395, Jul. 2011.

31. Davenport, M. A., D. Takhar, J. N. Laska, et al., "Single-pixel imaging via compressive sampling," *IEEE Signal Processing Magazine*, Vol. 25, No. 2, 83–91, Mar. 2008.

32. Wiaux, Y., L. Jacques, G. Puy, et al., "Compressed sensing

imaging techniques for radio interferometry," *Monthly Notices of the Royal Astronomical Society*, Vol. 395, No. 3, 1733–1742, May 2009.

33. McEwen, J. D. and Y. Wiaux, "Compressed sensing for radio interferometric imaging: Review and future direction," *IEEE International Conference on Image Processing*, 1313–1316, Sept. 2011.

34. Muthukrishnan, S., *Data Streams: Algorithms and Applications*, Now Publishers, Hanover, MA, 2005.

35. Yang, J. G., J. Thompson, X. T. Huang, et al., "Random-frequency SAR imaging based on compressed sensing," *IEEE Trans. Geoscience and Remote Sensing*, Vol. PP, No. 99, 1–12, 2012.

36. Becker, S., J. Bobin, and E. Candes, "NESTA: A fast and accurate first-order method for sparse recovery," *SIAM Journal on Imaging Sciences*, Vol. 4, No. 1, 1–39, 2011.

37. Tropp, J. A., A. C. Gilbert, and M. J. Strauss, "Algorithm for simultaneous sparse approximation. Part I: Greedy pursuit," *Signal Processing*, Vol. 86, 572–588, 2006.

38. Needell, D., "Topics in compressed sensing," Ph.D. Dissertation, Mathematics, University of California, Davis, May 2009.

39. Needell, D. and R. Vershynin, "Signal recovery from incomplete and inaccurate measurements via regularized orthogonal matching pursuit," *IEEE Journal of Selected Topics in Signal Processing*, Vol. 4, No. 2, 310–316, Apr. 2010.

40. Corbella, I., N. Duffo, M. Vall-llossera, et al., "The visibility function in interferometric aperture synthesis radiometry," *IEEE Trans. Geoscience and Remote Sensing*, Vol. 42, No. 8, 1677–1682, Aug. 2004.

41. Butora, R., M. Martín-Neira, and A. L. Rivada-Antich, "Fringe-washing function calibration in aperture synthesis microwave radiometry," *Radio Science*, Vol. 38, No. 2, 15-1–15-5, Apr. 2003.

42. Romberg, J., "Imaging via compressive sampling," *IEEE Signal Processing Magazine*, Vol. 25, No. 2, 14–20, Mar. 2008.

43. Tropp, J. and A. Gilbert, "Signal recovery from random measurements via orthogonal matching pursuit," *IEEE Trans. Information Theory*, Vol. 53, No. 12, 4655–4666, Dec. 2007.

44. Figueiredo, M. A. T., R. D. Nowak, and S. J. Wright, "Gradient projection for sparse reconstruction: Application to compressed sensing and other inverse problems," *IEEE Journal of Selected Topics in Signal Processing*, Vol. 1, No. 4, 586–597, Apr. 2007.

45. Wright, S. J., R. D. Nowak, and M. A. T. Figueiredo, "Sparse reconstruction by separable approximation," *IEEE Trans. Signal Processing*, Vol. 57, No. 7, 2479–2493, Jul. 2009.

46. Beck, A. and M. Teboulle, "Fast iterative shrinkage-thresholding algorithm for linear inverse problems," *SIAM Journal on Imaging Sciences*, Vol. 2, No. 1, 183–202, 2009.

47. Hale, E. T., W. Yin, and Y. Zhang, "Fixed-point continuation for ℓ_1 minimization: Methodology and convergence," *SIAM Journal on Optimization*, Vol. 19, No. 3, 1107–1130, 2008.

48. Nesterov, Y., *Introductory Lectures on Convex Optimization. A Basic Course*, Kluwer Academic Publishers, Boston, 2004.

49. Nesterov, Y., "Smooth minimization of non-smooth functions," *Math. Program. Ser. A*, Vol. 103, 127–152, 2005.

50. Nesterov, Y., "Gradient methods for minimizing composite objective function," Technical Report 2007/76, CORE, Université catholique de Louvain, Louvain-la-Neuve, Belgium, 2007.

51. Torres, F., A. B. Tanner, S. T. Brown, and B. H. Lambrigsten, "Robust array configuration for a microwave interferometric radiometer: Application to the GeoSTAR project," *IEEE Geoscience and Remote Sensing Letters*, Vol. 4, No. 1, 97–101, Jan. 2007.

52. Sutton, B. P., D. C. Noll, and J. A. Fessler, "Fast, iterative image reconstruction for MRI in the presence of field inhomogeneities," *IEEE Trans. Medical Imaging*, Vol. 22, No. 2, 178–188, Feb. 2003.

53. Bronstein, M. M., A. M. Bronstein, M. Zibulevsky, and H. Azhari, "Reconstruction in diffraction ultrasound tomography using nonuniform FFT," *IEEE Trans. Medical Imaging*, Vol. 21, No. 11, 1395–1401, Nov. 2002.

54. Yunyue, L., Y. Zhang, and J. Claerbout, "Hyperbolic estimation of sparse models from erratic data," *Geophysics*, Vol. 77, No. 1, V1–V9, 2012.